LOCAL BUCKLING OF RHS MEMBERS UNDER BIAXIAL BENDING AND AXIAL FORCE

Luís Vieira* Rodrigo Gonçalves** Dinar Camotim*

* CERIS, ICIST, DECivil, Instituto Superior Técnico, Universidade de Lisboa, 1049-001 Lisbon, Portugal
e-mails: luisjfvieira@hotmail.com, dcamotim@civil.ist.utl.pt

** CERIS, ICIST and Departamento de Engenharia Civil, Faculdade de Ciências e Tecnologia, Universidade Nova de Lisboa 2829-516 Caparica, Portugal
e-mail: rodrigo.goncalves@fct.unl.pt

Keywords: Local buckling, Rectangular hollow sections, Axial force, Biaxial bending, Axial force and biaxial bending, Generalized Beam Theory.

Abstract. *This paper aims at providing an in-depth analysis of the local plate buckling coefficients for thin-walled rectangular hollow sections (RHS) subjected to biaxial bending and/or axial force. For the determination of these coefficients, a computational efficient Generalised Beam Theory formulation is implemented in a MATLAB code, capable of calculating accurate local buckling loads with a very small computational cost and, therefore, making it possible to conduct extensive parametric studies in a very short period of time. Taking advantage of the small longitudinal half-wavelength nature of the local buckling mode, semi-analytical solutions using sinusoidal half-wave amplitude functions may be employed for the GBT cross-section deformation modes. The code then computes the lowest local buckling load by varying the member length and using the "golden-section search" algorithm. Although most of the paper is devoted to cross-sections without rounded corners, the code is also capable of handling rounded corners and a preliminary study concerning its effect on the buckling coefficients is also presented.*

1 INTRODUCTION

In the framework of the Research Fund for Coal and Steel project RFCS-2015-709892 – "Overall-Slenderness Based Direct Design for Strength and Stability of Innovative Hollow Sections – HOLLOSSTAB" – a study concerning the local (plate-like) buckling behaviour of rectangular hollow sections (RHS) was carried out by the authors. This study is motivated by the fact that the majority of the current steel design codes, including the European code [1], addresses this problem by assuming that all walls are hinged along their edges, meaning that they may buckle independently. This assumption is on the safe side, since the beneficial effect of the rotational restraint provided by the adjacent walls is discarded. However, this beneficial effect may be significant, as it depends on the cross-sectional stress distribution and geometric ratios (e.g. the cross-section height/width), leading to very significant changes in the local buckling coefficient k_σ, defined through

$$\sigma_{cr} = k_\sigma \frac{\pi^2 E}{12\left(1-v^2\right)} \left(\frac{t}{b}\right)^2 ,$$ (1)

where σ_{cr} is the critical stress, E is Young's Modulus, v is Poisson's ratio, b is the relevant wall width and t is its thickness. For RHS of constant thickness with negligible rounded corners, this coefficient can be related to the web ($b=h_w$) or to the flange ($b=b_f$), through

$$\sigma_{cr} = k_w \frac{\pi^2 E}{12(1-\nu^2)} \left(\frac{t}{h_w}\right)^2 = k_f \frac{\pi^2 E}{12(1-\nu^2)} \left(\frac{t}{b_f}\right)^2 , \qquad (2)$$

leading to

$$k_f = k_w \left(\frac{b_f}{h_w}\right)^2 . \qquad (3)$$

Although this effect of cross-section wall interaction can be explicitly accounted for through freely available numerical tools such as GBTUL [2] or CUFSM [3], not many studies are available concerning an accurate determination of the buckling coefficients for RHS members and all of them discard the effect of the rounded corners. In [4], charts are provided for the buckling coefficients of axially compressed tubes as a function of the cross-section geometric ratios (mid-line width/height and flange/web thickness ratios of 0.5,1 and 2). This problem is equally addressed in [5] and [6]. More recently, in [7], finite strip analyses were used to calculate the local buckling loads of the AISC database cross-section shapes, from which analytical expressions for the local buckling coefficient were proposed for members subjected to either axial compression, major axis bending or minor axis bending.

Recently, the authors have addressed the local buckling behavior of RHS members under combined axial and biaxial bending [8]. However, in this earlier work, the effect of rounded corners was not considered. The work presented in this paper aims at (i) presenting the main findings of [8], namely easy-to-use charts and closed-form analytical expressions for the local buckling coefficient of straight-edge RHS, considering a wide range of load cases, and (ii) showing some preliminary results concerning the effect of rounded corners.

To perform all the necessary calculations and parametric studies in a fast and reliable way, a numerical model based on the Generalised Beam Theory (GBT) was developed. GBT is a thin-walled bar theory that allows for cross-section in-plane and out-of-plane deformation through the consideration of so-called "cross-section deformation modes", whose longitudinal amplitude functions constitute the problem unknowns. GBT was initially introduced by Richard Schardt [9] and has been continuously developed since then. Presently, its efficiency is well-established, due to its ability (i) to obtain accurate and structurally enlightening solutions with just a few deformation modes (and thus just a few DOFs) and also (ii) to include or exclude specific effects in a very straightforward manner (see, e.g., [10,11] and the list of publications by the Lisbon-based research group at www.civil.ist.utl.pt/gbt).

The outline of the paper is as follows. Section 2 describes the numerical model developed for the calculation of the critical bifurcation loads. In Section 3, parametric analyses are conducted considering straight-edge RHS members. Both simple and complex loading arrangements, involving axial force and biaxial bending, are examined, disclosing the influence of the height-to-width and height-to-thickness ratios, as well as the importance of "non-Vlasov local" modes. The results are then compared with those available in the literature and used to plot charts and develop approximate analytical formulae to calculate the local buckling coefficient. Section 4 presents a preliminary study concerning the effect of the rounded corners. Finally, section 5 summarizes the main conclusions of the work carried out.

2 DESCRIPTION OF THE NUMERICAL MODEL

A GBT specialization is employed to determine the critical bifurcation loads of RHS members. First, the relevant cross-section modes are identified. Secondly, the critical bifurcation load for a given combination of axial force and biaxial bending is computed by means of a standard linear stability analysis procedure.

2.1 Deformation modes

Figure 1a shows the RHS geometric parameters adopted in this work. The cross-section corners may be rounded, as shown in Figure 1b. For simplicity, the following illustrations are based on the straight-edge model (the procedure is identical for either case). The cross-section global axes are Y and Z, defining the major and minor bending axes, respectively. The cross-section is discretized by subdividing each cross-section element (web, flange or corner) in straight walls of equal length. Figure 1c shows an example with two intermediate nodes in each web and one intermediate node in each flange. Mid-surface local axes (x, y, z) are set up in each wall, along which the corresponding displacements pertaining to each mode k are defined (u_k, v_k, w_k respectively). These displacement components are expressed as
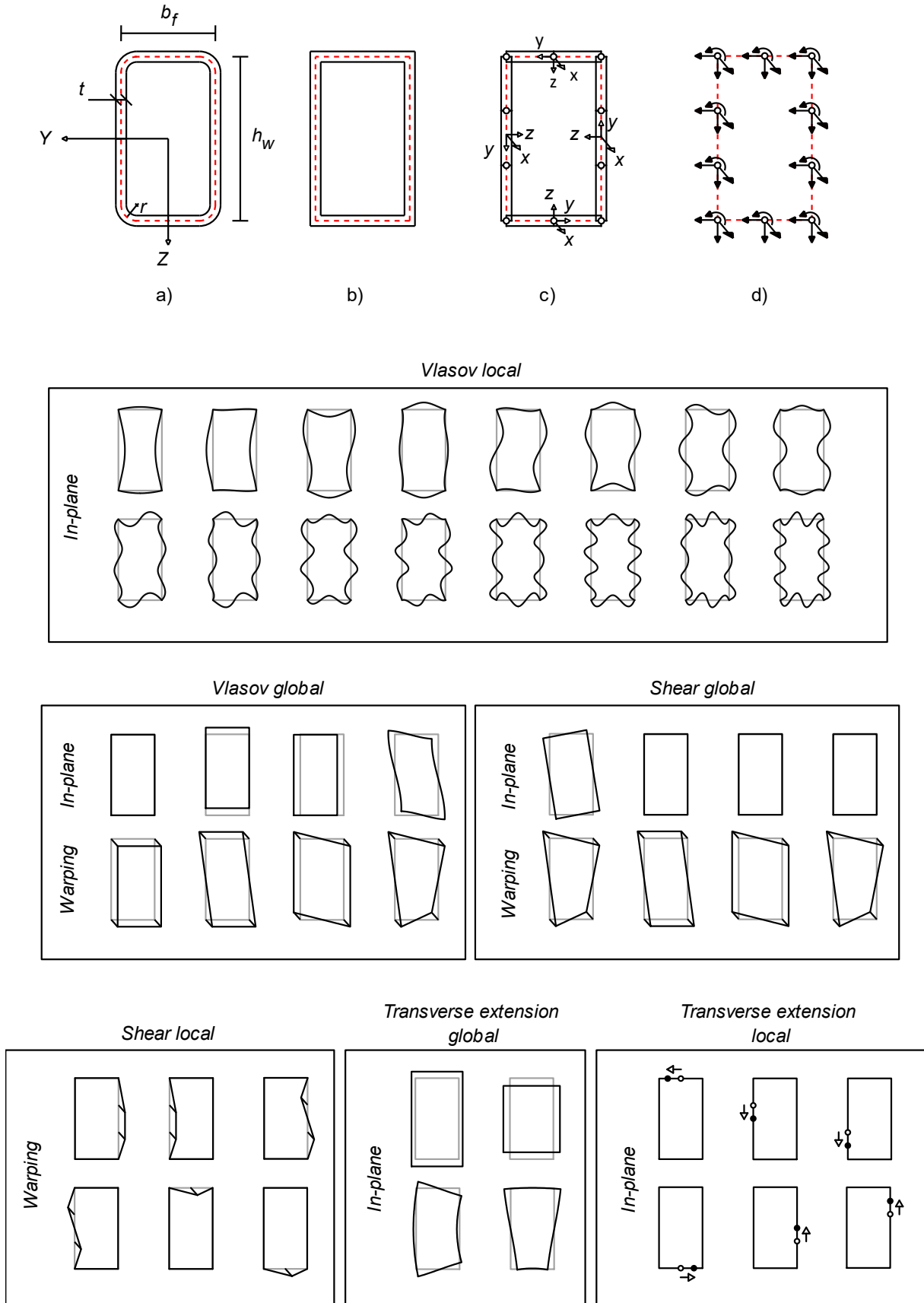
$$
\begin{aligned}
u_k &= \bar{u}_k(y)\phi_{k,x}(x), \\
v_k &= \bar{v}_k(y)\phi_k(x), \\
w_k &= \bar{w}_k(y)\phi_k(x),
\end{aligned}
\tag{4}
$$

where subscript commas indicate differentiation, $\bar{u}_k(y)$, $\bar{v}_k(y)$, $\bar{w}_k(y)$ are the deformation mode shape functions and $\phi_k(x)$ are the corresponding amplitude functions.

An initial deformation mode basis is generated by considering three displacements along the local axes and one cross-section in-plane rotation per node, as shown in Figure 1d. This leads to a deformation mode space with $4N$ modes, where N is the total number of nodes. Note that this procedure is somewhat different from the classic GBT one, where the in-plane rotations are statically condensed. The displacement functions $\bar{u}_k$ and $\bar{v}_k$ are approximated by means of Lagrange linear polynomials, whereas Hermite cubic functions are employed for $\bar{w}_k$.

The final deformation modes are calculated as explained in [12,13,14], although the in-plane nodal rotations are included in the present case. This process is based on solving a set of eigenvalue problems, involving pairs of GBT modal linear and geometric stiffness matrices (see Eqs. (5) and (7) below), where the deformation modes correspond to the calculated eigenvectors. The modes are shown in Figure 1e and can be subdivided into three distinct sets:

  (i) *Vlasov modes*, which have null membrane shear strains (Vlasov's assumption) and null membrane transverse extensions: four global modes (axial extension, two bending modes and one distortional mode) and several local modes, depending on the wall discretization. If the corners are rounded, the local modes will no longer have null in-plane displacements at the wall junctions and, furthermore, they involve warping displacements, as described in [15];

  (ii) Shear modes (non-null membrane shear strains): four global modes (torsion and the warping functions of the Vlasov bending/distortional modes) and several local warping modes (depending on the wall discretization);

  (iii) Transverse extension modes (non-null membrane shear strains and transverse extensions): four global modes and several local modes (depending on the wall discretization).

a)   b)   c)   d)

Vlasov local

In-plane

Vlasov global   *Shear global*

In-plane

Warping

In-plane

Warping

Shear local   *Transverse extension global*   *Transverse extension local*

Warping

In-plane

In-plane

e)

Figure 1: a) Geometry of rounded RHS, b) equivalent straight-edge RHS, c) discretization of the equivalent straight-edge RHS, d) initial DOFs and e) Deformation mode space.

In general, the local buckling of RHS members can be accurately predicted by the Vlasov local modes, but other modes may participate in the solution. For this reason, two variants of the GBT formulation were employed in the present work: (1) only Vlasov local modes and (2) all modes (totalling 4*N* modes). Variant 2 is the most accurate and simultaneously the most expensive from a computational point of view (particularly for refined cross-section discretizations), but makes it possible to assess the error associated with considering only the Vlasov local-plate modes.

For Variant 1, in which only the Vlasov local modes are employed, a rather fast procedure can be devised using the GBT modal linear stiffness matrices, which read (e.g., [12])

$$B_{ij} = B_{ij}^M + B_{ij}^B = \int_S \frac{Et}{1-v^2} \bar{v}_{i,y} \bar{v}_{j,y} \, dy + \int_S \frac{Et^3}{12(1-v^2)} \bar{w}_{i,yy} \bar{w}_{j,yy} \, dy,$$

$$C_{ij} = C_{ij}^M + C_{ij}^B = \int_S \frac{\alpha Et}{1-v^2} \bar{u}_i \bar{u}_j \, dy + \int_S \frac{Et^3}{12(1-v^2)} \bar{w}_i \bar{w}_j \, dy, \tag{5}$$

$$D_{1ij} = D_{1ij}^M + D_{1ij}^B = \int_S Gt(\bar{u}_{i,y} + \bar{v}_i)(\bar{u}_{j,y} + \bar{v}_j)dy + \int_S \frac{Gt^3}{3} \bar{w}_{i,y} \bar{w}_{j,y} dy,$$

where the *M* and *B* superscripts designate membrane and bending terms, respectively, *G* is the shear modulus and $\alpha = 1$ if the deformation modes include wall transverse extensions and $\alpha = (1-v^2)$ otherwise.

The Vlasov local modes are calculated using the following fast procedure:

1. The shear and transverse extension modes are removed by calculating the 2*N* dimension basis of the nullspace of $\left(\mathbf{D}_1^M + \mathbf{B}^M\right)$, which corresponds to the Vlasov modes (null membrane shear strains and null membrane transverse extensions).
2. The local modes are the $\lambda \neq 0$ eigenvectors of $\mathbf{B}^B \mathbf{v} = \lambda \mathbf{C} \mathbf{v}$, except for the first one, which corresponds to distortion (the lowest non-null eigenvalue).

Sinusoidal amplitude functions of the form $\phi_k(x) = \bar{\phi}_k \sin(\pi x/L)$, where *L* is the half-wavelength and $\bar{\phi}_k$ is the mode amplitude, constitute the exact solutions for simply supported members and lead to the bifurcation equation [12]

$$\left(\frac{\pi^2}{L^2} \mathbf{C} + \mathbf{D} + \frac{L^2}{\pi^2} \mathbf{B} + \lambda \left(\mathbf{X}_1 + \frac{\pi^2}{L^2} \mathbf{X}_2\right)\right) \bar{\phi} = \mathbf{0}, \tag{6}$$

where λ is the load parameter, and $\mathbf{D}, \mathbf{X}_1$ and $\mathbf{X}_2$ are linear and geometric stiffness matrices, which read

$$\mathbf{D} = \mathbf{D}_1 - \mathbf{D}_2 - \mathbf{D}_2^\mathsf{T},$$

$$D_{2ij} = D_{2ij}^M + D_{2ij}^B = \int_S \frac{vEt}{1-v^2} \bar{v}_{i,y} \bar{u}_j \, dy + \int_S \frac{vEt^3}{12(1-v^2)} \bar{w}_{i,yy} \bar{w}_j \, dy, \tag{7}$$

$$X_{1ij} = \int_S \sigma(\bar{v}_i \bar{v}_j + \bar{w}_i \bar{w}_j) \, dy,$$

$$X_{2ij} = \int_S \sigma(\bar{u}_i \bar{u}_j) \, dy,$$

where σ is the longitudinal normal stress along the cross-section mid-line. The buckling eigenvalue problem (6) is computationally very efficient, since the number of DOFs equals the number of deformation modes included in the analysis. However, the calculation of the half-wavelength that corresponds to the minimum critical bifurcation load parameter requires an iterative strategy. In this work, the golden-section search algorithm was employed [16].

The code was implemented in MATLAB [17]. Numerical integration was performed using 4 Gauss points, which is exact given the approximation functions used. With an Intel Core i7-4710HQ @ 2.50GHz processor, the runtime for nearly 14000 analyses, each with 320 DOFs, is about 6 minutes.

3. PARAMETRIC STUDY FOR STRAIGHT-EDGE RHS

3.1 Introduction

A total of 124 RHS cross-sections were analysed, with h_w/b_f values between 1 and 4, with a step of 0.1, and b_f/t values ranging from 10 to 40, with a step of 10, which is in agreement with most standard commercial cross-sections. The cross-sections were modelled as straight-edge (as shown in Figure 1b) and simplified to their centreline. Fig. 2 shows a convergence analysis, indicating that for axial compression and uniaxial bending, a subdivision of each wall into 5 segments (four intermediate nodes) leads to results within 0.2% of those obtained with 10 intermediate nodes.
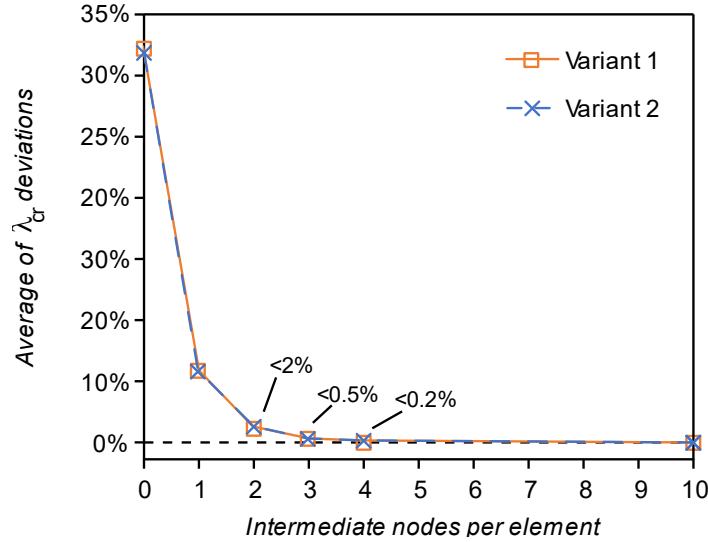
Figure 2: Maximum absolute deviation of the critical buckling stress for all cross-sections, under *N*, M_y or M_z, with respect to those obtained with ten intermediate nodes per wall

The two variants presented in Section 2 are considered (analyses with the Vlasov local modes only or with all modes). Finally, several load combinations are addressed:
- o simple individual loadings, namely axial force (*N*), major axis bending (M_z) or minor axis bending (M_z);
- o combined loadings, namely $N+M_y$, $N+M_z$, M_y+M_z and $N+M_y+M_z$.

Table 1 shows a statistical summary of the differences in the results obtained with the two variants concerning several loading combinations involving axial force and biaxial bending. It is possible to observe a reduction of the critical buckling stress (which is proportional to the buckling coefficients) when all modes are considered, which strongly correlates with the b_f/t ratio. Although not shown, both variants were validated through comparisons with results obtained with GBTUL [2] and CUFSM [3]. Noteworthy differences are obtained for b_f/t =10 only, which corresponds to rather stocky cross-sections, where behaviour is not governed by local buckling phenomena[1]. For higher b_f/t ratios, the accuracy is on average below 1%, with a small standard deviation. It is therefore acceptable to consider only the Vlasov local modes in the calculations. This approximation is very relevant, as it makes the buckling coefficients independent of the b_f/t ratio. For this reason, the following analyses are carried out with Variant

---

[1] For example, according to [20], the minimum width-to-thickness ratio for which an internal compression part is unable to develop its full plastic capacity equals $38\sqrt{235/f_y}$, where f_y is the yield stress in MPa. This limit is well above 10 even for high strength steel grades.

1, making the buckling coefficients dependent only on (i) the stress distribution and (ii) the h_w/b_f ratio.

Table 1: Reduction in critical buckling coefficients considering Variant 2 instead of Variant 1.

	$\dfrac{b_f}{t} = 10$	$\dfrac{b_f}{t} = 20$	$\dfrac{b_f}{t} = 30$	$\dfrac{b_f}{t} = 40$
Min	-11.1%	-2.5%	-1.1%	-0.6%
Max	-0.1%	-0.0%	-0.1%	-0.0%
Average	-2.9%	-0.7%	-0.3%	-0.2%
Std. Dev	1.4%	0.3%	0.2%	0.1%

In Section 3.2 the influence of h_w/b_f for simple loadings (axial compression, major or minor axis bending) is investigated, in which case the results can be compared with those available in literature. In Section 3.3, combined loading cases are analysed, namely (i) axial compression with uniaxial bending, (ii) biaxial bending and (iii) axial force with biaxial bending. Finally, in Section 3.4, charts and analytical expressions to determine the local buckling coefficient are proposed. For readability purposes, the results concerning complex loading cases are presented for $h_w/b_f= 1$, 2, 3 and 4 only, as more detailed results can be found in [8].

3.2. Local buckling under simple loading cases

The graphs in Figures 3, 4 and 5 show the variation of both web and flange buckling coefficients with h_w/b_f, for axial compression, major and minor axis bending, respectively. In these figures, various buckling modes are also provided, scaled such that the web maximum displacement is constant.

For axial compression (Figure 3), the results coincide with those in [4], and differ slightly from those obtained with the analytical expressions provided in [7].. For major and minor axis bending, the proposed procedure and [7] provide similar buckling coefficients (see Figures 4 and 5).

The influence of h_w/b_f on k_w and k_f is noticeably dependent on the stress distribution. In the case of an axially compressed square tube, all walls are subject to uniform stresses and necessarily one has $k_w = k_f = 4.0$ (the result for simply supported square plates). By increasing h_w/b_f, web buckling becomes increasingly restrained by the flange, resulting in an increase in k_w. At the same time, from Eq. (3), k_f necessarily decreases.

For minor axis bending, one of the webs is under uniform compressive stresses, whereas the flanges are subjected to a linear stress diagram. Buckling is mostly driven by the compressed web and thus the h_w/b_f ratio has a minute influence on k_w. For major axis bending, in sections close to SHS, the compressed flange governs and therefore k_f does not vary strongly. However, in sections with high h_w/b_f, local buckling is triggered by the web linear compressive stresses and leads to a reduction of k_f.
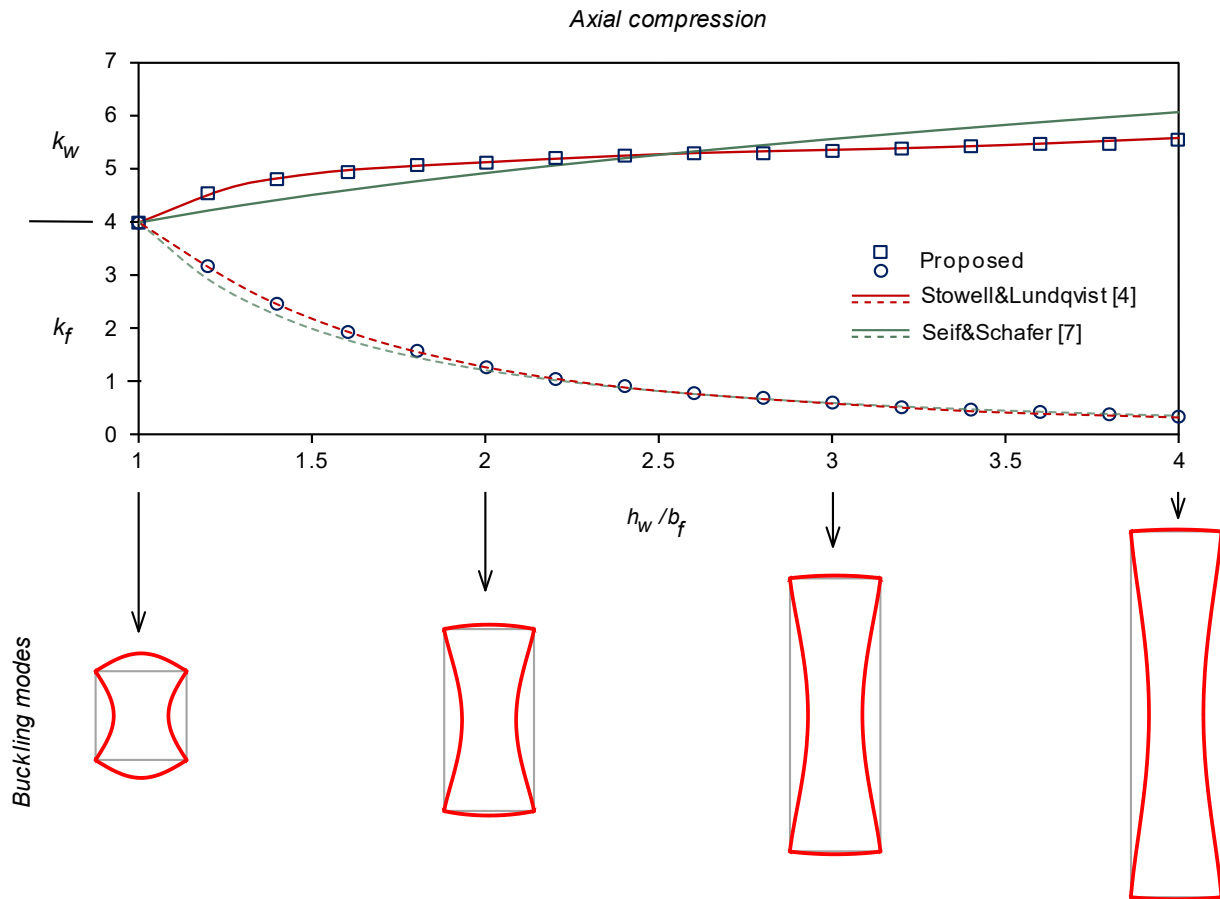
Axial compression

Figure 3: Buckling coefficients and modes for axial compression.
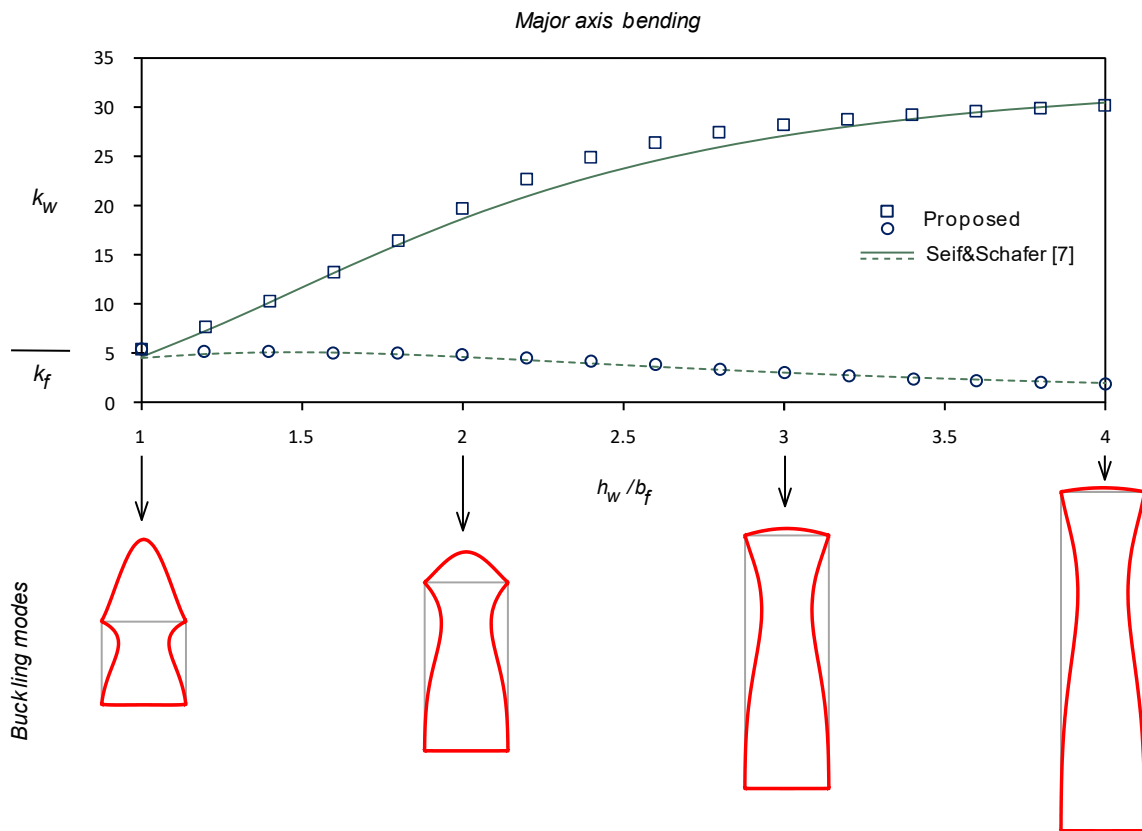
Major axis bending

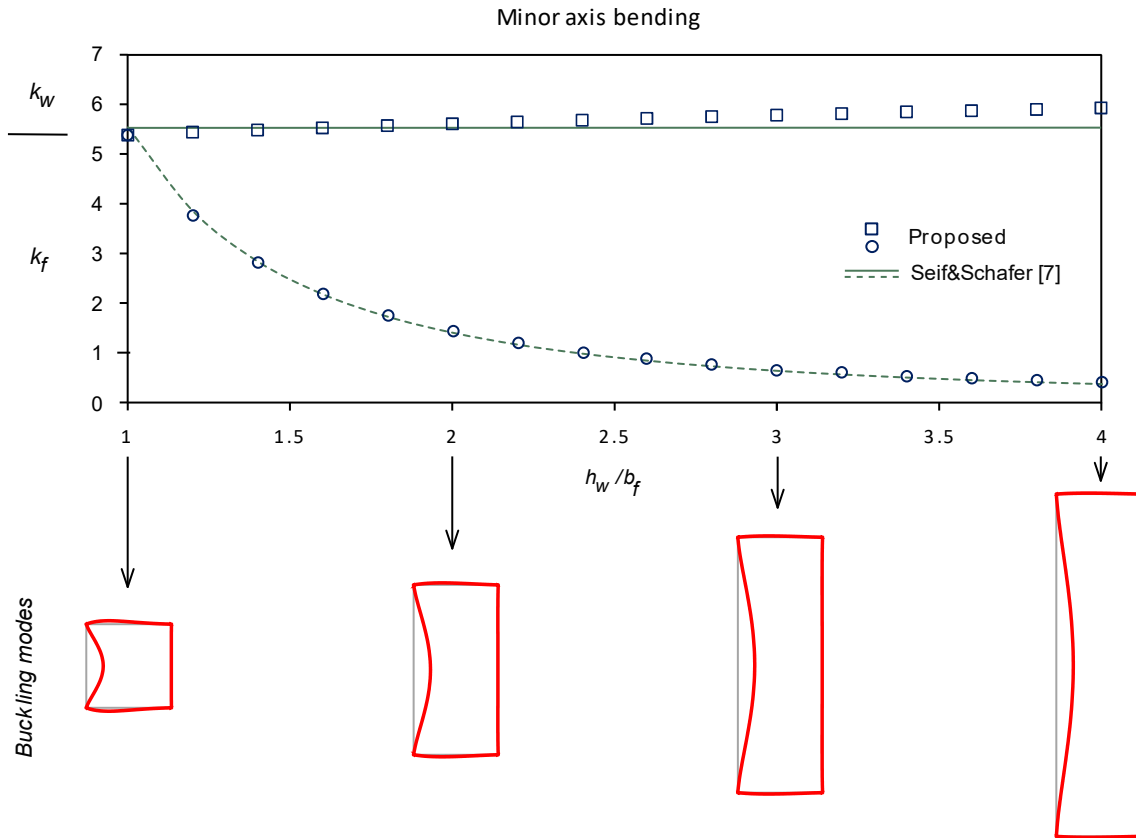Figure 4: Buckling coefficients and modes for major axis bending.

Figure 5: Buckling coefficients and modes for minor axis bending.

Overall, it is observed that, as h_w/b_f increases, buckling tends to be governed by the webs and not the flanges. For a given stress distribution, an increase in this ratio causes an increase in the relation between the web and flange compressed widths. At the same time, the flanges offer more restraint to the rotation of the corners. In fact, by analysing cross-sections with much higher h_w/b_f values, it can be observed that k_w tends asymptotically to the value for built-in plates (6.97 for a fully compressed web and 39.6 for a web under bending [18]). The flange buckling coefficients, on the other hand, obviously tend to zero (see Figure 6).
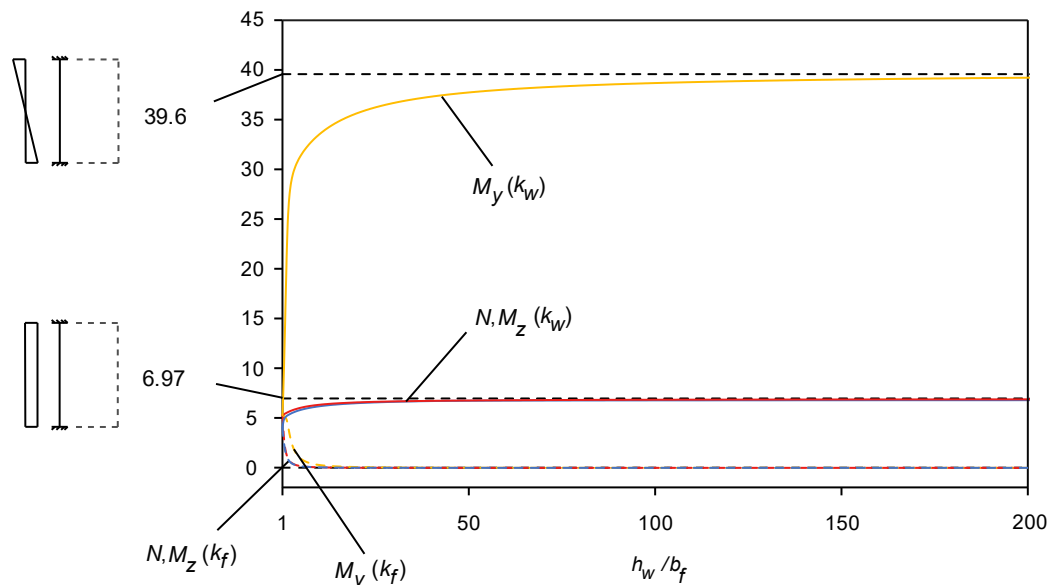

Figure 6: Variation of k_w/k_f with h_w/b_f for a RHS under N, M_y or M_z.

3.3 Local buckling under combined loading

For combined loading the stress distribution may be parametrized using the arbitrary cross-section distribution shown in Figure 7 and

$$\psi_w = \frac{\sigma_B}{\sigma_A}, \qquad \psi_f = \frac{\sigma_C}{\sigma_A}, \tag{8}$$

where ψ_w, $\psi_f \in [-1,1]$ and point A corresponds to the web-flange midline corner where the higher compressive stress occurs (in the present work, the webs always refer to the wider cross-section walls).
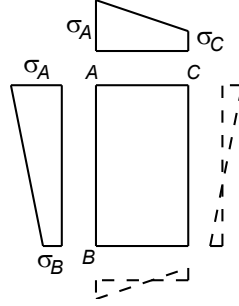
Figure 7: Normal stress distribution in a RHS under combined axial force and biaxial bending.

To enable a better understanding on how the stress profile relates to the critical local buckling, from here onwards reference is made only to k_w, since instability is generally driven by web buckling. However, recall that k_f may be easily retrieved from Eq.(3).

3.3.1 Axial compression and uniaxial bending

For axial compression and major axis bending ψ_w varies and $\psi_f = 1$, whereas for axial compression and minor axis bending the opposite occurs. The variation of k_w with ψ_w and ψ_f, for selected values of h_w/b_f, and the most relevant buckling modes are displayed in Figures 8 and 9. It is observed that for narrower cross-sections (increasing values of h_w/b_f), the differences between the various curves become smaller. The same was observed already for axial compression and uniaxial bending, which constitute "boundary cases" and for which it was shown that, as h_w/b_f increases, the k_w curves tend to a horizontal line. It should be noted that the minimum and maximum k_w values are obtained for axial compression and uniaxial bending, respectively. The increase in the lower value of the linear stress diagram (which corresponds to moving from M_y or M_z to N) is necessarily associated with a lower buckling load, since there is a global increase in compressive stresses which makes the cross-section more susceptible to buckling. This can be attested by observing Figures 8 and 9 (the maximum web displacement of the buckling modes is kept constant): the critical local buckling coefficients decrease as one approaches axial compression.

The variations of the buckling mode shape with ψ_w and ψ_f are visibly distinct for $h_w/b_f = 1$ and $h_w/b_f = 4$. Unlike in the SHS, where the transition between instability shapes appears to be gradual, for the narrow RHS the buckling modes associated with $\psi_w/\psi_f = 0$ and 1 are nearly identical and involve displacements much higher in the webs than in the flanges.
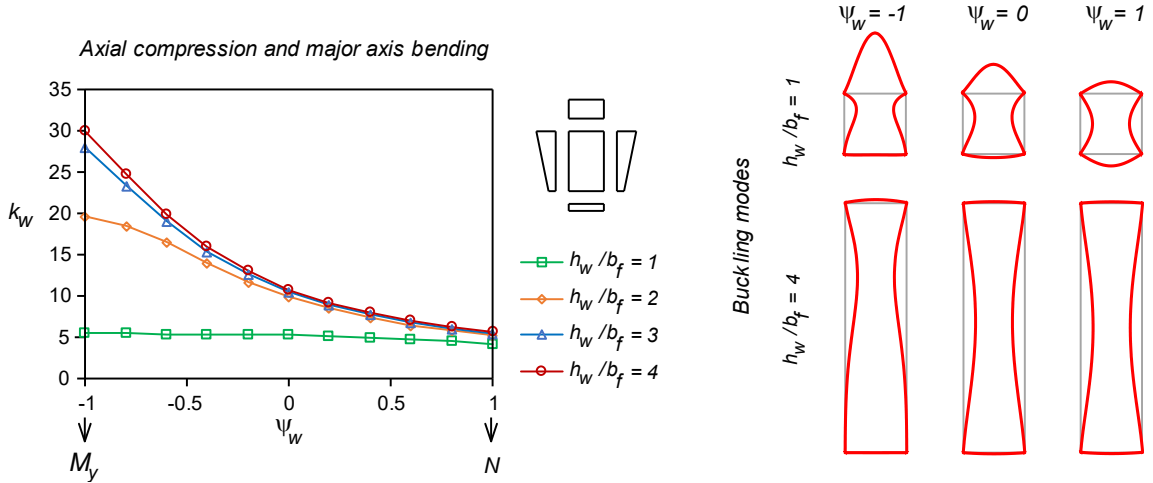
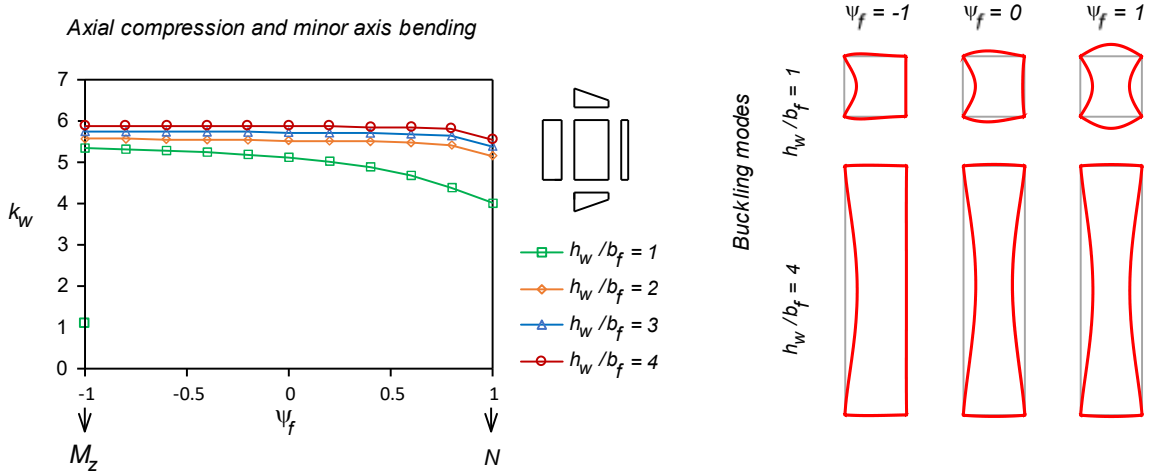Figure 8: Axial compression and major axis bending.

Figure 9: Axial compression and minor axis bending.

3.3.2 Biaxial bending

For biaxial bending both ψ_w and ψ_f may vary, but one has $\psi_w = -\psi_f$. The variation of k_w with h_w/b_f and the most relevant buckling modes are displayed in Figure 10. It is observed that as one moves from major to minor axis bending (i.e., ψ_w moves from -1 to 1), the k_w values for different h_w/b_f converge to approximately 5. It is also worth noting that the minimum k_w value is always obtained for minor axis bending ($\psi_f = -1$ or, for a square tube, also $\psi_f = 1$). Conversely, as h_w/b_f increases, the maximum k_w is obtained for increasing ψ_f values. In particular, this maximum value is attained for $\psi_f = 0$, for a SHS, and for $\psi_f = -1$ if $h_w/b_f \geq 3$. The variation of the buckling modes follows a similar trend to that described regarding axial compression and uniaxial bending.
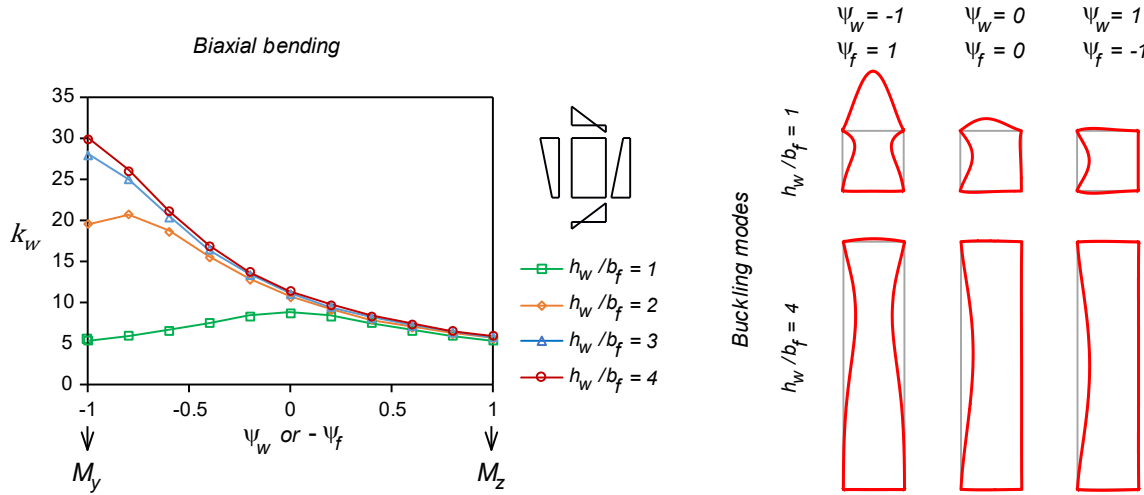
Figure 10: Biaxial bending.

3.3.3 Combined axial force and biaxial bending

Combined axial force and biaxial bending constitutes the most general loading case. Figure 12 shows the web buckling coefficients obtained for different h_w/b_f values, displayed as (ψ_w, ψ_f) surface plots and corresponding contour lines. To enable a better grasp of the following results and those presented earlier, Figure 11 identifies, in this 2D space, the "boundary cases" addressed so far. Note that $\psi_w < -\psi_f$ indicates that $N > 0$.
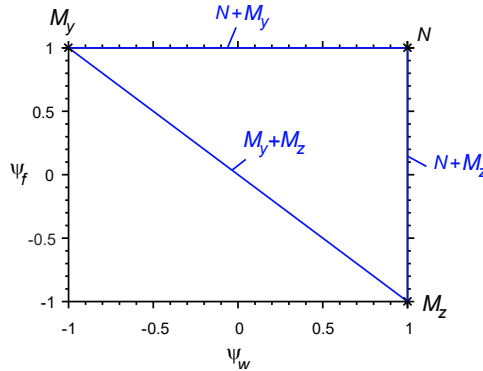

Figure 11: Identification of the load combinations in the (ψ_w, ψ_f) 2D space.

Both the surface and contour plots were obtained from curve-fitting of the web buckling coefficients obtained for (ψ_w, ψ_f) pairs defining a mesh with intervals of 0.1 along both directions. The MATLAB griddata method was used, which employs biharmonic spline interpolation.

It is observed that the buckling coefficient increases as ψ_w and/or ψ_f decreases, in agreement with the previous findings. For SHS, the surfaces are naturally symmetric with respect to the $\psi_w = \psi_f$ axis and, for increasingly narrower RHS, they become mostly dependant on ψ_w. This transition agrees with the gradual shift of the maximum k_w for biaxial bending towards lower ψ_w (see also Figure 10). Also note that, even for the highest cross-section ratio considered, k_w decreases as ψ_f approaches 1.
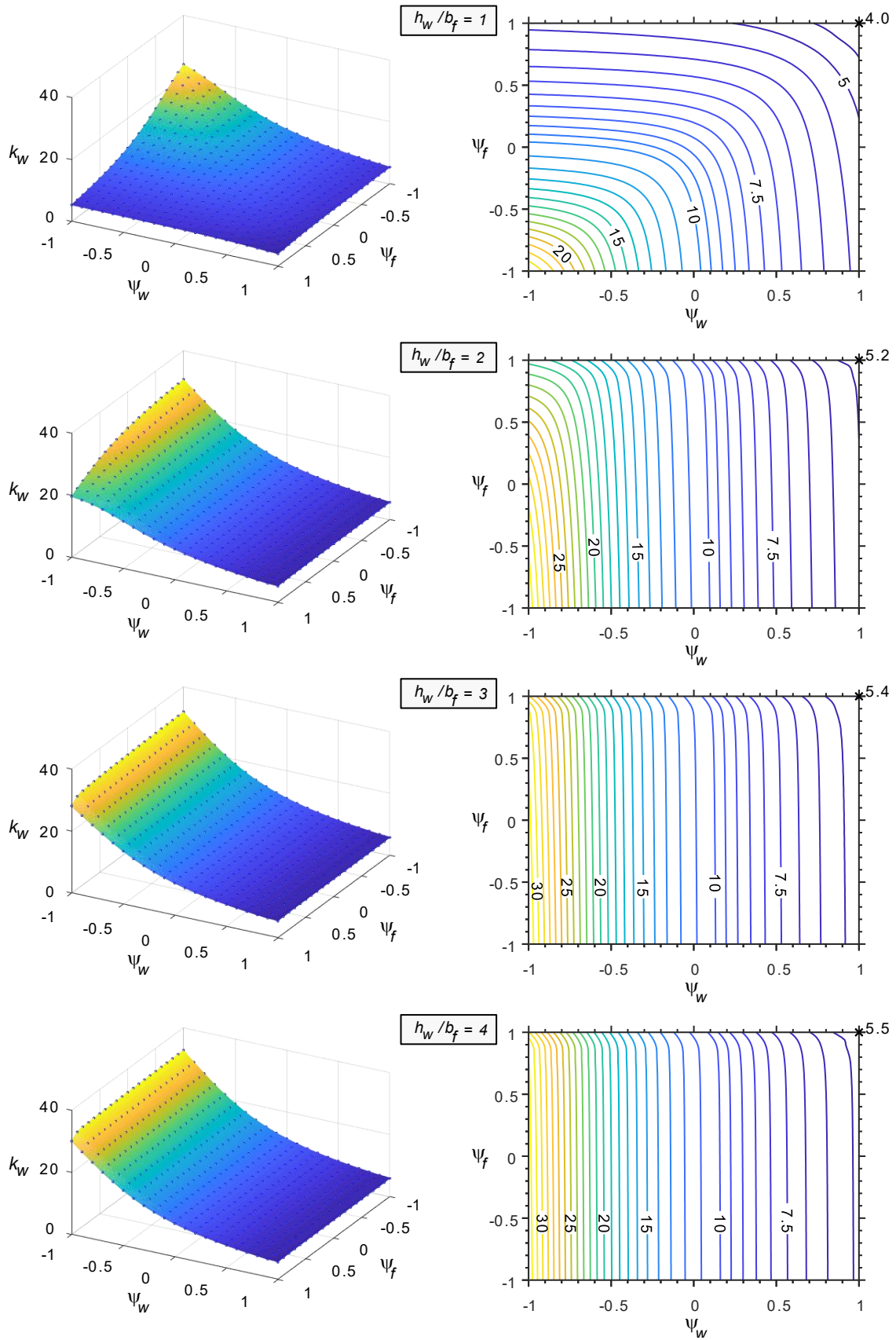
Figure 12: k_w curve-fitted surface plots and contour lines for axial force and biaxial bending

3.4 Approximate formulae

With the results obtained in the previous sections, approximate expressions were developed for combined axial force and biaxial bending. The weighted linear least squares method was used, employing increasingly higher-order polynomials until correlation was deemed satisfactory. Instead of using ψ_w and ψ_f directly as input parameters, shifted coordinates $\psi'_w = \psi_w - 1$ and $\psi'_f = \psi_f - 1$ were adopted, since this simplifies considerably the resulting polynomials. Table 2 displays the proposed formulae for k_w and Table 3 provides the relevant coefficients as a function of the h_w/b_f ratio. Note that the main and the cross-order coefficients are of the 4th and 5th degree, respectively, and that $p_{00} = k_w$ for axial compression. Finally, Table 4 provides a summary of the statistical regression information, showing that accurate results are obtained for the parameter ranges considered.

Table 2: k_w formulae for different load cases.

	k_w
$N\text{-}M_y\text{-}M_z$	$p_{00} + \sum_{i=1}^{4}\left(p_{i0}(\psi_w - 1)^i + p_{0i}(\psi_f - 1)^i\right) + \sum_{i=1}^{4}\sum_{j=1}^{5-i} p_{ij}(\psi_w - 1)^i(\psi_f - 1)^j$
N	p_{00}
$N\text{-}M_y$	$p_{00} + \sum_{i=1}^{4} p_{i0}(\psi_w - 1)^i$
$N\text{-}M_z$	$p_{00} + \sum_{i=1}^{4} p_{0i}(\psi_f - 1)^i$

Table 3: Polynomial coefficients for the definition of k_w.

h_w/b_f	p_{00}	p_{01}	p_{02}	p_{03}	p_{04}	p_{10}	p_{20}	p_{30}	p_{40}
1	4.000	-2.230	-1.585	-0.543	-0.070	-2.230	-1.585	-0.543	-0.070
2	5.158	-1.571	-2.396	-1.497	-0.322	-4.488	-6.436	-9.368	-2.727
3	5.384	-1.554	-2.432	-1.528	-0.329	-3.895	-3.141	-5.076	-0.822
4	5.541	-1.549	-2.445	-1.540	-0.333	-3.853	-2.577	-4.414	-0.518

h_w/b_f	p_{11}	p_{21}	p_{12}	p_{31}	p_{22}	p_{13}	p_{41}	p_{32}	p_{23}	p_{14}
1	-1.373	-2.837	-2.837	0.018	-3.005	0.018	0.561	-0.945	-0.945	0.561
2	0.101	-2.660	1.592	-2.906	0.681	0.607	-1.489	0.473	0.141	0.021
3	1.574	-0.847	3.887	-0.081	-1.112	3.343	-0.285	0.323	-0.553	0.928
4	1.575	-0.665	3.816	0.219	-1.127	3.261	-0.081	0.183	-0.463	0.884

Table 4: Statistical information concerning the analytical formulas relative to the numerical model

h_w/b_f	$N\text{-}M_y$				$N\text{-}M_z$				$N\text{-}M_y\text{-}M_z$			
	Max	Min	Mean	Std. Dev.	Max	Min	Mean	Std. Dev.	Max	Min	Mean	Std. Dev.
1	0.3%	-0.2%	0.0%	0.1%	0.3%	-0.1%	0.0%	0.1%	2.7%	-6.0%	-1.0%	2.2%
2	0.5%	-0.9%	-0.1%	0.4%	2.5%	-1.5%	0.2%	1.1%	2.5%	-4.0%	-0.9%	1.3%
3	0.5%	-0.9%	-0.1%	0.4%	1.6%	-1.0%	0.1%	0.8%	2.1%	-2.8%	0.0%	1.0%
4	0.5%	-0.9%	-0.1%	0.4%	1.4%	-0.9%	0.1%	0.7%	2.0%	-2.8%	0.0%	1.0%

4. THE EFFECT OF ROUNDED CORNERS

This section presents a preliminary study concerning the effect of rounded corners on the critical buckling coefficients of RHS under axial force, major axis bending or minor axis bending. The cross-section database of EN10219-Part 2 [19] is employed. The mean radii are computed in accordance with these specifications, reproduced in Table 5. According to these rules, some of the cross-sections are very compact, with very narrow flat parts, and can hardly be considered thin-walled. Out of the entire set of cross-sections, the cases in which the flat wall width is lower than 10 times the thickness were discarded, leading to a total of 188 cross-sections to analyse.

Table 5: Rules for determination of the mean corner radii

Thickness (t)	External corner radius (r_o)	Internal corner radius (r_i)	Mean corner radius ($r = (r_o + r_i)/2$)
$t \leq 6$ mm	2.0t	1.0t	1.5t
6 mm $< t \leq 10$ mm	2.5t	1.5t	2.0t
10 mm $< t$	3.0t	2.0t	2.5t

4.1 Definition of the buckling coefficients in RHS with rounded corners

For RHS with rounded corners, the highest stress may be found at the corner, rendering the calculations somewhat complex. To avoid this case, new coefficients $\overline{k_w}$ and $\overline{k_f}$ are introduced, which relate to a fictitious stress $\overline{\sigma_{cr}}$, found by "extending" the stress distribution to the intersection of the most compressed web and flange mid-lines, as shown in Figure 13:

$$\overline{\sigma_{cr}} = \overline{k_w} \frac{\pi^2 E}{12(1-v^2)} \left(\frac{t}{h_w}\right)^2 = \overline{k_f} \frac{\pi^2 E}{12(1-v^2)} \left(\frac{t}{b_f}\right)^2 . \tag{9}$$
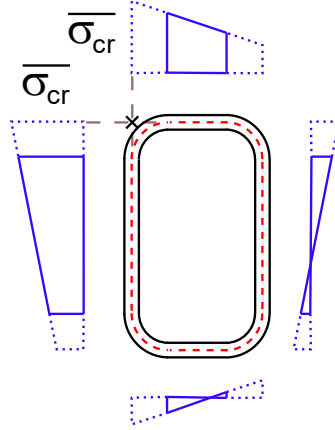

Figure 13: Calculation of the fictitious stress $\overline{\sigma_{cr}}$.

Naturally, the previous results for k_w and k_f pertaining to straight edges are no more than a particular case of $\overline{k_w}$ and $\overline{k_f}$ when the radius is null.

The effect of the rounded corners may be assessed by means of the coefficient R_k, reading

$$R_k = \frac{\overline{k_w}}{k_{w,str-edge}} = \frac{\overline{k_f}}{k_{f,str-edge}} , \tag{10}$$

where the subscript "*str-edge*" corresponds to a cross-section with the same geometry but with straight edges. With this coefficient it is possible to relate the critical load parameter of the two sections through

$$\overline{\lambda_{cr}} = R_k \lambda_{cr,str-edge}. \tag{11}$$

4.2 Local buckling under simple loading cases

As in Section 3, analyses were first carried out using Variants 1 (only Vlasov local modes) and 2 (all modes), to assess the relevance of the non-Vlasov local modes. Figures 14, 15 and 16 show the $\overline{k_w}$ results for axial compression, major axis bending and minor axis bending and the corresponding R_k values for the two Variants, as well as the web buckling coefficients for straight-edge RHS determined with Variant 2.
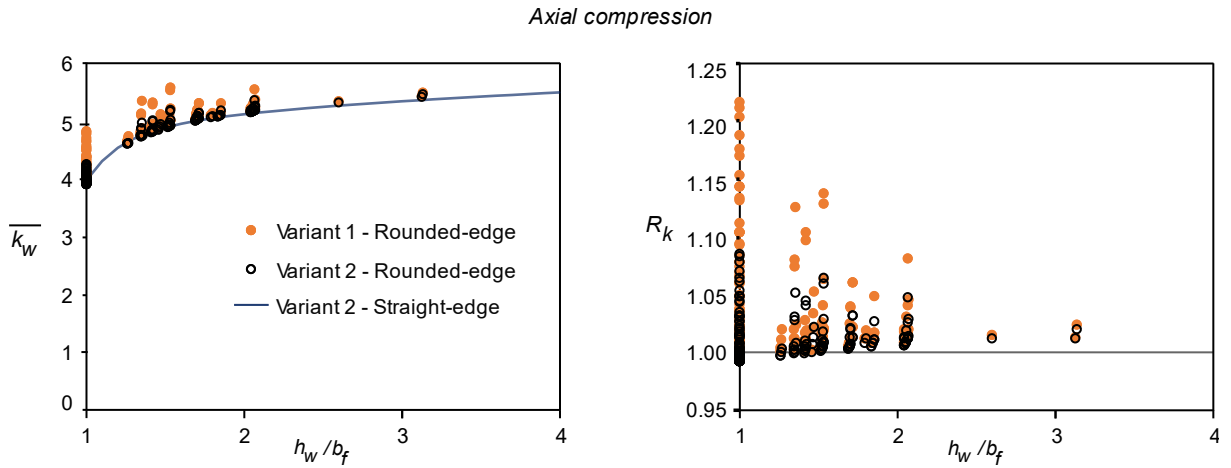

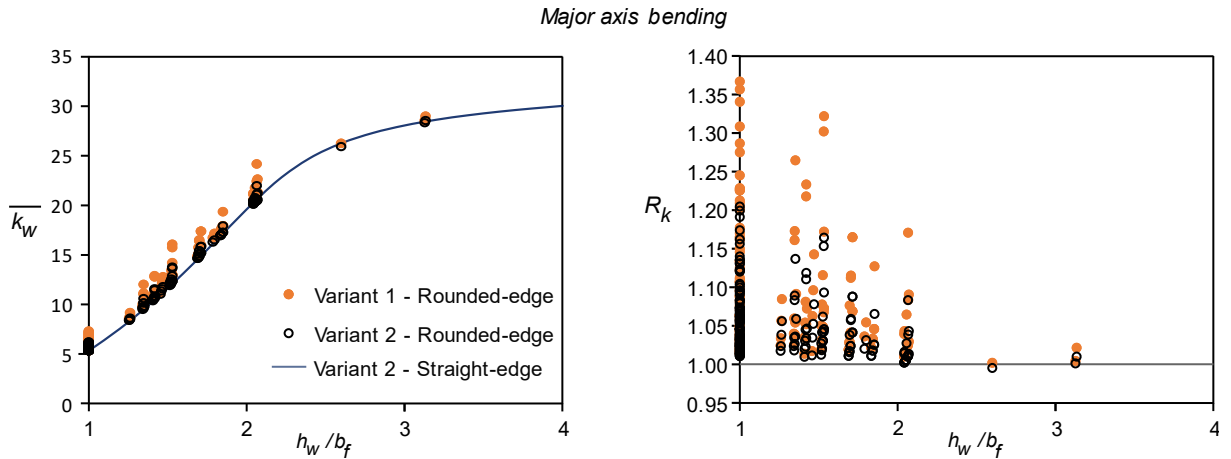Figure 14: $\overline{k_w}$ and R_k for rounded-edge RHS under axial compression.

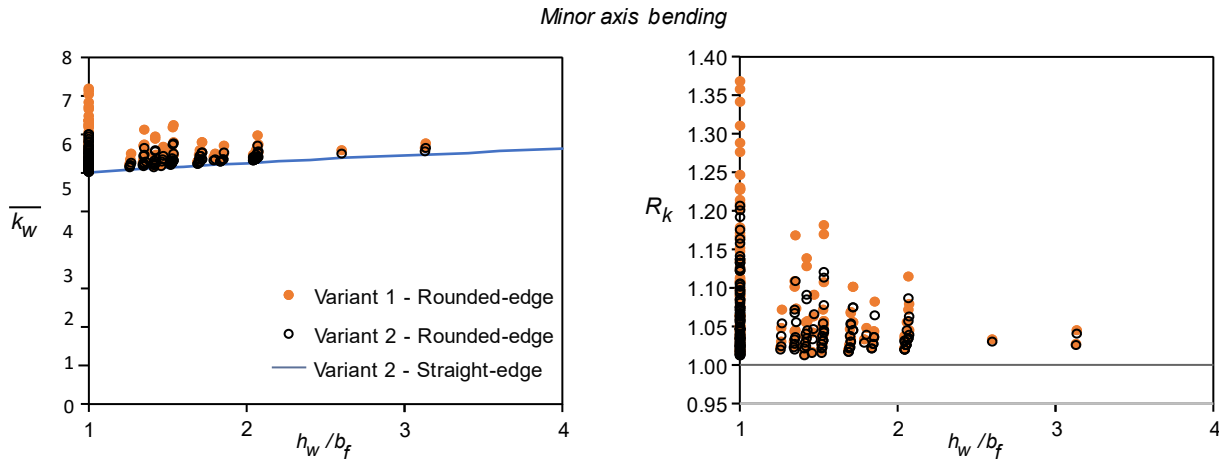Figure 15: $\overline{k_w}$ and R_k for rounded-edge RHS under major axis bending.

Figure 16: $\overline{k_w}$ and R_k for rounded-edge RHS under minor axis bending.

From these three load cases, two conclusions can be withdrawn:

(i) With rounded corners, the buckling coefficient $\overline{k_w}$ increases for almost every case and for both variants (thus implying that $R_k > 1$), namely for SHS. This is due to a stiffening effect caused by the reduction of the flat portions of the webs/flanges and also the fact that the buckling mode involves significant membrane warping, as shown in Figure 17 (this warping vanishes for straight edges).

(ii) The non-Vlasov local modes play an important role in the local buckling behaviour for RHS with rounded corners, since their inclusion in the analyses leads to lower values of $\overline{k_w}$ (and R_k). This shows that the local buckling behaviour of RHS with rounded corners is much more complex than that for RHS with straight edges (note in Figure 17 that the local buckling modes no longer have null in-plane displacements of the wall junctions).
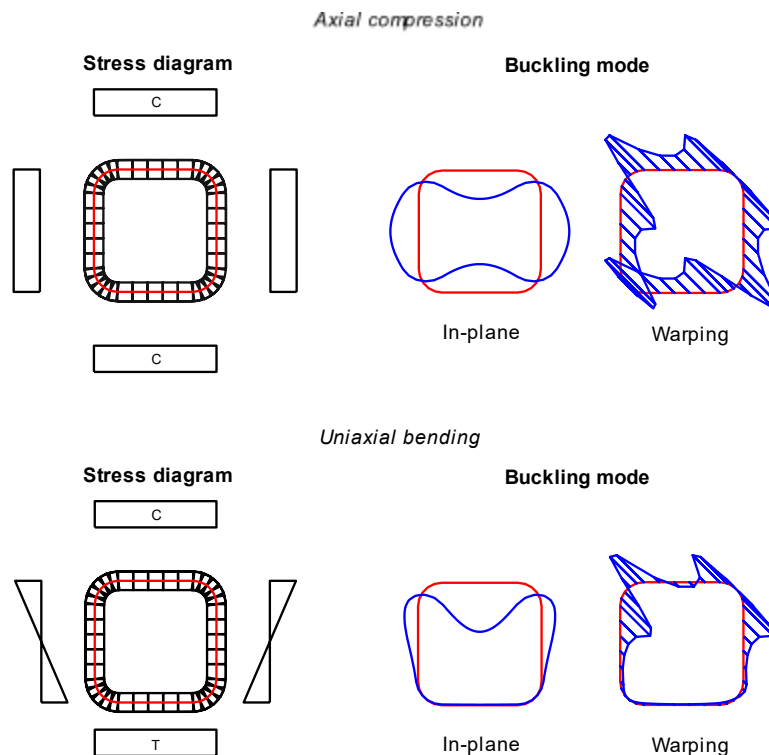

Figure 17: Buckling modes for a rounded-edge SHS under axial compression and uniaxial bending.

Lastly, the influence of the mid-line corner radius is investigated considering the results obtained with Variant 2. The graphs in Figure 18 plot R_k, for the selected values of the radius-to-thickness ratio, as a function of the parameter $(h_w+b_f)/r$, which takes lower values as the corner radius increases with respect to the equivalent straight-edge cross-section mid-line dimensions. The results show that there is a tendency for R_k to increase as the relative size of the corners increases, particularly for the cases of major and minor axis bending, in which case a trend is most evident and R_k reaches higher values. Although there is still a slight scatter, it can be reduced by subdividing the results in each graph according to the corresponding *r/t* ratio, which shows that this parameter is also relevant.
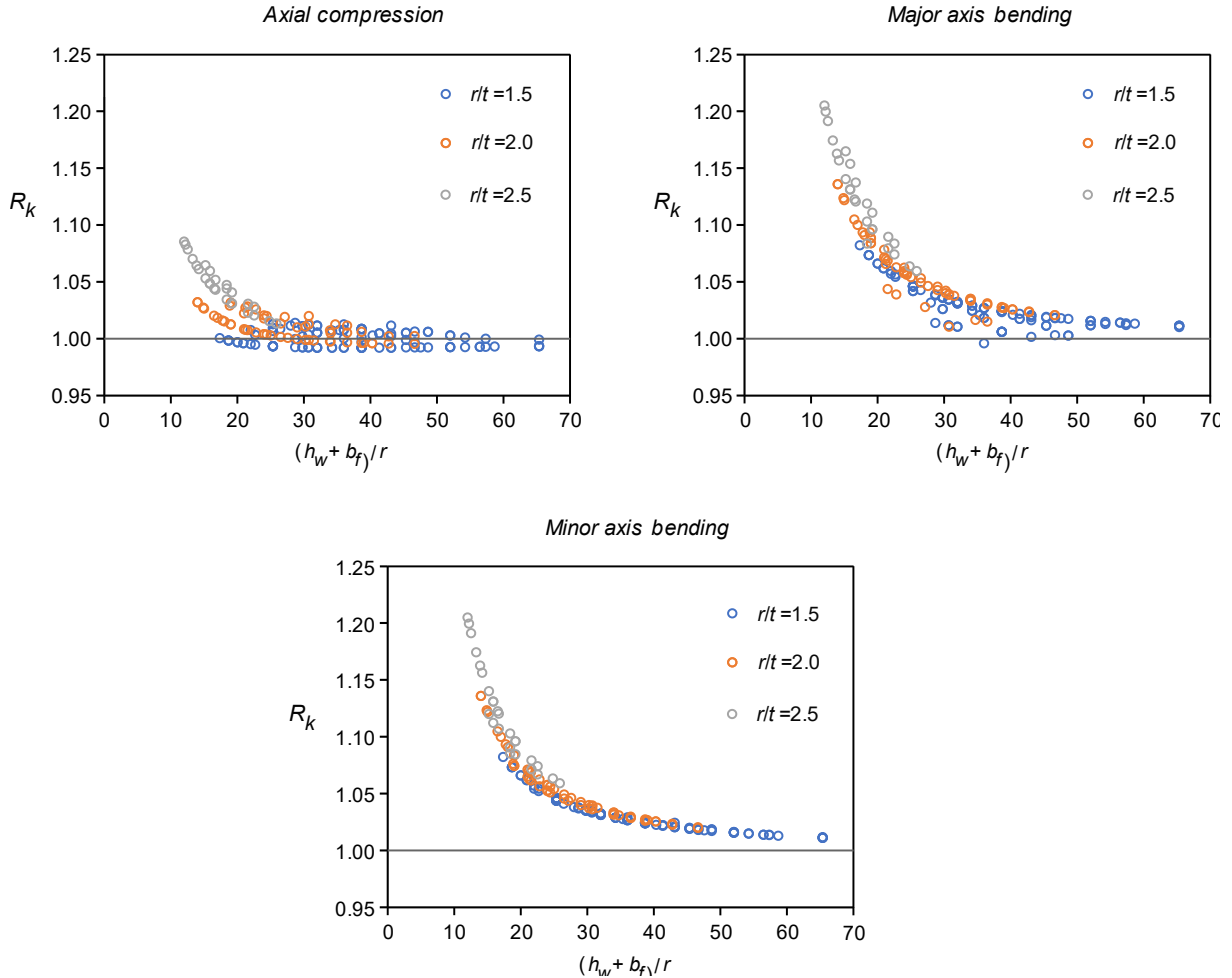

Figure 18: Influence of the corner radius to the coefficient R_k

5 CONCLUSION

This paper assessed the local buckling behaviour of thin-walled RHS members subjected to combinations of axial load, major and minor axis bending. The minimum critical local buckling loads were calculated by means of a computationally efficient GBT specialization for RHS.

For straight edges, the results showed that the inclusion of the Vlasov local deformation modes in the buckling analysis is sufficient to provide accurate bifurcation loads for non-compact cross-sections. This simplification made it possible to perform analyses considering only (i) the cross-section normal stress distribution and (ii) the mid-line height-to-width ratio (h_w/b_f). The results obtained with the proposed model agree very well with those available in literature for either axial compression, major or minor axis bending. The cases of combined (i)

axial compression and uniaxial bending, (ii) biaxial bending and (iii) combined axial force and biaxial bending, were handled for the first time. For each case, charts and approximate analytical expressions obtained through curve-fitting techniques were presented.

For rounded corners, it was shown that the buckling modes are significantly more complex and that an accurate calculation of the critical buckling load requires including all sets of GBT cross-section deformation modes in the analysis. Moreover, it was demonstrated that, with respect to the straight edge case, the buckling loads increase due to a stiffening of the cross-section resulting from the reduction of the flat portion of the cross-section and the occurrence of significant membrane warping.

Further studies are currently under way to investigate the effect of rounded corners for RHS subjected to arbitrary loading.

REFERENCES

[1]   CEN, *EN 1993-1-5. Eurocode 3 : Design of Steel Structures - Part 1-5: Plated structural elements*. 2006.

[2]   R. Bebiano, D. Camotim, and R. Gonçalves, "GBTUl 2.0 − A second-generation code for the GBT-based buckling and vibration analysis of thin-walled members", *Thin-Walled Struct.*, 124, 235–257, 2018.

[3]   Z. Li and B. W. Schafer, "Buckling analysis of cold-formed steel members with general boundary conditions using CUFSM: Conventional and constrained finite strip methods", *Proceedings of the Twentieth International Specialty Conference on Cold-Formed Steel Structures*, 17-31, 2010.

[4]   E. Z. Stowell and E. E. Lundquist, "Local Instability of Columns with I-, Z-, Channel, and Rectangular-Tube Sections", *Natl. Advis. Comm. Aeronaut. Washington, D.C, U.S.A.*, 1939.

[5]   F. Bleich, *Buckling strength of metal structures*, McGraw-Hill, New York, 1952.

[6]   H. G. Allen and P. S. Bulson, *Background to buckling*, McGraw-Hill, London, 1980.

[7]   M. Seif and B. W. Schafer, "Local buckling of structural steel shapes", *J. Constr. Steel Res.*, 66(10), 1232–1247, 2010.

[8]   L. Vieira, R. Gonçalves, and D. Camotim, "On the local buckling of RHS members under axial force and biaxial bending", *Thin-Walled Structures*, 129, 10–19, 2018.

[9]   R. Schardt, *Verallgemeinerte Technische Biegetheorie*, Springer-Verlag, Berlin, 1989.

[10] D. Camotim, N. Silvestre, R. Gonçalves, and P. B. Dinis, "GBT-based Structural Analysis of Thin-walled members: Overview, Recent Progress and Future Developments", *Adv. Eng. Struct. Mech. Constr.*, 140, 187–204, 2006.

[11] D. Camotim, C. Basaglia, R. Bebiano, R. Gonçalves, and N. Silvestre, "Latest developments in the GBT analysis of thin-walled steel structures", *Proceedings of the International Colloquium on Stability and Ductility of Steel Structures*, 2010.

[12] R. Gonçalves, M. Ritto-Corrêa, and D. Camotim, "A new approach to the calculation of cross-section deformation modes in the framework of generalized beam theory", *Comput. Mech.*, 46(5), 759–781, 2010.

[13]   R. Gonçalves, R. Bebiano, and D. Camotim, "On the Shear Deformation Modes in the Framework of Generalised Beam Theory", *Thin-Walled Structures*, 84, 325–334, 2014.

[14]   R. Bebiano, R. Gonçalves, and D. Camotim, "A cross-section analysis procedure to rationalise and automate the performance of GBT-based structural analyses", *Thin-Walled Structures*, 92, 29–47, 2015.

[15]   R. Gonçalves and D. Camotim, "GBT deformation modes for curved thin-walled cross-sections based on a mid-line polygonal approximation", *Thin-Walled Structures*, 103, 231–243, 2016.

[16]   J. Kiefer, "Sequential Minimax Search for a Maximum", *Proc. Am. Math. Soc.*, 4(3), 502, 1953.

[17]   The MathWorks Inc., "MATLAB." Natick, Massachussets, 2017.

[18]   T.V. Galambos, *Guide to Stability Design Criteria for Metal Structures*, T.V. Galambos (ed.), New York, John Wiley & Sons, Inc., 1988.

[19]   CEN, *EN 10219-2 Cold formed welded structural hollow sections of non-alloy and fine grain steels - Part 2: Tolerances, dimensions and sectional properties*. 2006.

[20]   CEN, *EN 1993-1-1. Eurocode 3 : Design of Steel Structures - Part 1-1: General Rules and Rules for Buildings*. 2005.